ELECTROMAGNETIC SUBSURFACE REMOTE SENSING

Subsurface electromagnetic (EM) methods are applied to obtain underground information that is not available from surface observations. Since electrical parameters such as dielectric permittivity and conductivity of subsurface materials may vary dramatically, the response of electromagnetic waves can be used to map the underground structure. This technique is referred to as geological surveying. Another major application of subsurface EM methods is to detect and locate underground anomalies such as mineral deposits.

Subsurface EM methods include a variety of techniques depending on the application, surveying method, system, and interpretation procedure, and thus a "best" method simply does not exist. Even though each system has its own characteristics, they still share some common features. In general, each system has a transmitter, which can be either natural or artificial, to send out the electromagnetic energy that serves as an input signal. A receiver is needed to collect the response signal. The underground can be viewed as a system, which is characterized by the material parameters and underground geometry. The task of subsurface EM methods is to derive the underground information from the response signal.

The EM transmitter radiates the primary field into the subsurface, which consists of conductive earth material. This primary field will induce a currents, which in turn radiates a secondary field. Either the secondary field or the total field will be detected by the receiver. After the data interpretation, one can obtain the underground information.

One of the most challenging parts of subsurface EM methods is interpretation of the data. Since the incident field interacts with the subsurface in a very complex manner, it is never easy to subtract the information from the receiver signal. Many definitions, such as apparent conductivity, are introduced to facilitate this procedure.

Data interpretation is also a critical factor in evaluating the effectiveness of the system. How good the system is always depends on how well the data can be explained. In the early development of subsurface EM systems, data interpretation largely depended on the personal experience of the operator, due to the complexity of the problem. Only with the aid of powerful computers and improvements in computational EM techniques is it possible to analyze such a complicated problem in a reasonable time. Computer-based interpretation and inversion methods are attracting more and more attention. Nevertheless, data interpretation is still "an artful balance of physical understanding, awareness of the geological constraints, and pure experience" (1).

In the following sections, we will use several typical applications to outline the basic principles of subsurface EM methods. Physical insight is emphasized rather than rigorous mathematical analysis. Details of each method can be found in the references.

BOREHOLE EM METHODS

Borehole EM methods are an important part of well-logging methods. Since water is conductive and oil is an insulator, resistivity measurements are good indicators of oil presence. Water has an unusually high dielectic constant, and permittivity measurement is a good detector of moisture content.

Early borehole EM methods consist of mainly electrical measurements using very simple low-frequency electrodes like the short and the long normal. Then more sophisticated electrode tools were developed. Some of these tools are mounted on a mandrel, which performs measurements centered in a borehole. These tools are called mandrel tools. Alternatively, the sensors can be mounted on a pad, and the corresponding tool is called a pad tool.

One of the most successful borehole EM methods is induction logging. Since Doll published his first paper in 1949 (2), this technique has been used widely with confidence in the petroleum industry. Extensive research work has been done in this area. The systems in use now are so sophisticated that many modern electrical techniques are involved. Nevertheless, the principles still remain the same and can be understood by studying a simple case.

The induction logging technique, as proposed by Doll, makes use of several coils wound on an isolating mandrel, called a sonde. Some of the coils, referred to as transmitters, are powered with alternating current (ac). The transmitters radiate the field into the conductive formation and induce a secondary current, which is nearly proportional to the formation conductivity. The secondary current radiates a secondary field, which can be detected by the receiver coils. The receiver signal (voltage) is normalized with respect to the transmitter current and resprented as an apparent conductivity, which serves as an indication of underground conductivity.

To obtain information from the apparent conductivity, we need to understand how apparent conductivity and true conductivity are related. According to Doll's theory, the relation in cylindrical coordinates is given by

$$\sigma_a = \int_{-\infty}^{+\infty} dz' \int_0^{+\infty} d\rho' g_{\mathrm{D}}(\rho', z')\sigma(\rho', z') \tag{1}$$

where σ_a is the formation conductivity. The kernel $g_{\mathrm{D}}(\rho, z)$ is the so-called Doll's geometrical factor, which weights the contribution of the conductivity from various regions in the vicinity of sonde.

We notice that $g_{\mathrm{D}}(\rho, z)$ is not a function of the true conductivity and hence is only determined by the tool configuration. The interpretation of the data would be simple if Doll's theory were exact. Unfortunately, this is rarely the case. Further studies show that Eq. (1) is true only in some extreme cases. The significance of Doll's theory, however, is that it relates the apparent conductivity and formation conductivity, even though the theory is not exact. In the early development of induction logging techniques, tool design and data interpretation were based on Doll's theory, and in most cases it gives reasonable answers.

To establish a firm understanding of induction logging theory, we need to perform a rigorous analysis by using Maxwell's equations as follows:

$$\nabla \times \boldsymbol{H} = -i\omega\epsilon\boldsymbol{E} + \boldsymbol{J}_{\mathrm{s}} + \sigma\boldsymbol{E} \tag{2}$$

$$\nabla \times \boldsymbol{E} = i\omega\mu\boldsymbol{H} \tag{3}$$

$$\nabla \cdot \boldsymbol{H} = 0 \tag{4}$$

$$\nabla \cdot \boldsymbol{D} = \rho \tag{5}$$

where $\nabla \cdot \boldsymbol{J}_{\mathrm{s}} = i\omega\rho$.

In the preceding equations, the time dependence $e^{-i\omega t}$ is assumed, and $\boldsymbol{J}_{\mathrm{s}}$ corresponds to the impressed current source. Parameters μ, ϵ, σ are the magnetic permeability, dielectric permittivity, and electric conductivity, respectively. To simplify the analysis, we assume that both the impressed source and geometry of the problem are axisymmetric; consequently, all the field components are independent of the azimuthal angle. Furthermore, it can be shown that there is no stored charge under the preceding assumption. The working frequency of induction logging is about 20 kHz, so the displacement current $-i\omega\epsilon\boldsymbol{E}$ is very small compared to the conduction current $\sigma\boldsymbol{E}$ and hence is neglected in the following discussion. After these simplifications, we have

$$\nabla \times \boldsymbol{H} - \sigma\boldsymbol{E} = \boldsymbol{J}_{\mathrm{s}} \tag{6}$$

$$\nabla \times \boldsymbol{E} - i\omega\mu\boldsymbol{H} = 0 \tag{7}$$

$$\nabla \cdot \boldsymbol{H} = 0 \tag{8}$$

$$\nabla \cdot \boldsymbol{E} = 0 \tag{9}$$

where we assume $\nabla \cdot \boldsymbol{J}_{\mathrm{s}} = i\omega\rho = 0$.

For convenience, the auxiliary vector potential is introduced. Since $\nabla \cdot \boldsymbol{H} = 0$ and $\nabla \cdot (\nabla \times\ ) = 0$, it is possible to define $\boldsymbol{H} = \nabla \times \boldsymbol{A}$. To specify the field uniquely, we choose $\boldsymbol{E} = i\omega\mu\boldsymbol{A}$, which is only true when there is no charge accumulation. Substituting these expressions into Eq. (6), we have

$$\nabla \times \nabla \times \boldsymbol{A} - i\omega\mu\sigma\boldsymbol{A} = \boldsymbol{J}_{\mathrm{s}} \tag{10}$$

By using the vector identity, we have

$$\nabla^2\boldsymbol{A} + k^2\boldsymbol{A} = -\boldsymbol{J}_{\mathrm{s}} \tag{11}$$

where

$$k^2 = i\omega\mu\sigma \tag{12}$$

To demonstrate how the apparent conductivity and formation conductivity are related, we first write down the solution of Eq. (11) in a homogeneous medium as follows (3,4):

$$\boldsymbol{A}(\rho, z, \phi) = \frac{1}{4\pi}\int_{V'} \frac{\boldsymbol{J}_{\mathrm{s}}(\rho', z', \phi')}{\overline{r}_1} e^{ik\overline{r}_1}\, dV' \tag{13}$$

where

$$\overline{r}_1 = \{(z-z')^2 + \rho^2 + \rho'^2 - 2\rho\rho'\cos(\phi - \phi')\}^{1/2} \tag{14}$$

The volume integration is evaluated over regions containing the impressed current sources and the coordinate system used in Eq. (13), as shown in Fig. 1. Usually, a small current

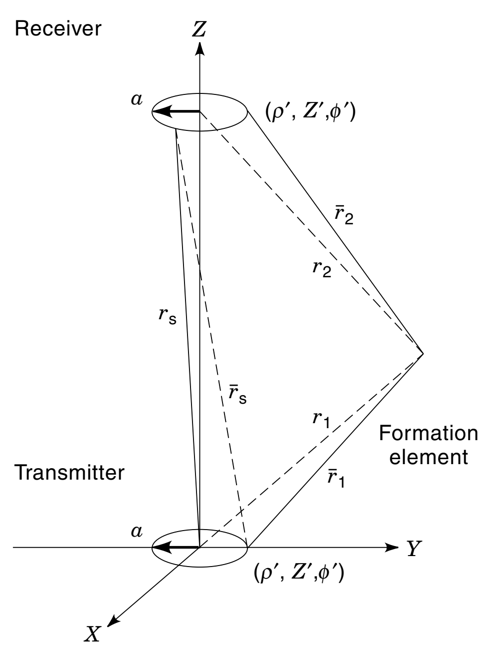

Figure 1. Induction logging tool transmitter and receiver coil pair used to explain the geometric factor theory. (Redrawn from Ref. 4.)

loop is used as an excitation, which implies that only $A\phi$ exists. Hence, Eq. (13) can be furthermore simplified as

$$A_\phi(\rho, z) = \frac{1}{4\pi}\int_{V'} \boldsymbol{J}_\phi(\rho', z')\cos(\phi - \phi')\frac{e^{ik\bar{r}_1}}{\bar{r}_1}\,dV' \qquad (15)$$

When the radius of the current loop becomes infinitely small, it can be viewed as a magnetic dipole and thus the preceding integration can be approximated as

$$A_\phi = \frac{m}{4\pi}\frac{\rho}{r_1^3}(1 - ikr_1)e^{ikr_1} \qquad (16)$$

where $m = N_T I(\pi a^2)$ is the magnetic dipole moment and N_T is the number of turns wound on the mandrel. At the receiver point, the voltage induced on the receiver with N_R turns can be represented as

$$\begin{aligned} V &= 2\pi a N_r E_\phi \\ &= \frac{2N_T N_R(\pi a^2)^2 I}{4\pi} i\omega\mu(1 - ikL)\frac{e^{ikL}}{L^3} \end{aligned} \qquad (17)$$

where

$$E_\phi = i\omega\mu A_\phi(a, L) \qquad (18)$$

and L is the distance between the transmitter and receiver. Since the voltage is a complex quantity, it can be separated into real and imaginary parts and expanded in powers of kL as follows (3):

$$V_R = -K\sigma\left(1 - \frac{2}{3}\frac{L}{\delta} + \cdots\right) \qquad (19)$$

$$V_X = K\sigma\frac{\delta^2}{L^2}\left(1 - \frac{2}{3}\frac{L^2}{\delta^3} + \cdots\right) \qquad (20)$$

where

$$K = \frac{(\omega\mu)^2(\pi a^2)^2}{4\pi}\frac{N_T N_R I}{L} \qquad (21)$$

and

$$\delta = \sqrt{\frac{2}{\omega\mu\sigma}} \qquad (22)$$

The quantity K is known as the tool constant and is totally determined by the configuration of the tool, and σ is the so-called skin depth, which describes the attenuation of a conductor in terms of the field penetration distance. The quantity V_R is called the R signal. The apparent conductivity is defined as (3)

$$\sigma_a = -\frac{V_R}{K} \cong \sigma\left(1 - \frac{2}{3}\frac{L}{\delta}\right) \qquad (23)$$

In the preceding analysis, there are some important facts that need to be mentioned. In Eq. (19), we see that the apparent conductivity is a nonlinear function of the true conductivity, even in a homogeneous medium. The lower the working frequency or lower the true conductivity, the more linear it will be. The difference between true conductivity and apparent conductivity is defined as the skin effect signal,

$$\sigma_s = \sigma - \sigma_a \qquad (24)$$

The leading term of the imaginary part V_X is not a function of true conductivity. In fact, it corresponds to the direct coupling field, which does not contain any formation information. What remains in V_X is the so-called X signal. Since the direct term is much larger than the residual part including V_R, it is difficult to separate the X signal. The importance of the X signal is seen by comparing Eqs. (19) and (20), from which we find that the X signal is the first-order approximation of the nonlinear term in V_R, the R signal. This fact can be used to compensate for the skin effect.

So far we have introduced the concept of apparent conductivity by studying the homogeneous case. In practice, the formation conductivity distribution is far more complicated. The apparent conductivity and formation conductivity are related through a nonlinear convolution. As a proof we derive the solution in an integral form, instead of directly solving the differential equations. To this end, we first rewrite Eq. (11) as

$$\nabla^2\boldsymbol{A} = -\boldsymbol{J}_s - \boldsymbol{J}_i \qquad (25)$$

where $\boldsymbol{J}_i = -k^2\boldsymbol{A}$ is the induced current. The solution of Eq. (25) can be written in the integral form as

$$\boldsymbol{A} = \frac{1}{4\pi}\int_{V'}\frac{\boldsymbol{J}_s}{\bar{r}_s}\,dV' + \frac{1}{4\pi}\int_V \frac{\boldsymbol{J}_i}{\bar{r}_2}\,dV \qquad (26)$$

The first integral is evaluated over the regions containing the impressed sources, and the second one is performed over the entire formation. Under the same assumption as we have made in the preceding analysis, the receiver voltage can be written as (4)

$$\begin{aligned} V = {} & \frac{i2\pi a N_R\omega\mu}{4\pi}\int_{V'}\frac{J_\phi}{\bar{r}_s}\,dV' \\ & - \frac{2\pi a N_R\omega^2\mu^2}{4\pi}\int_V \frac{\sigma(\rho', z')A_\phi(\rho', z')}{\bar{r}_2}\,dV \end{aligned} \qquad (27)$$

The vector potential can also be separated into real and imaginary parts:

$$A_\phi = A_{\phi R} + iA_{\phi I} \qquad (28)$$

Substituting Eq. (28) into Eq. (27) and separating out the real part of the receiver voltage, we have

$$\begin{aligned} V_R = {} & \frac{-(\omega\mu)^2(2\pi a N_R)}{4\pi}\int_{-\infty}^{\infty} dz' \int_0^\infty \\ & d\rho'\sigma(\rho', z')A_{\phi R}\int_0^{2\pi}\frac{\cos(\phi - \phi')}{\bar{r}_2}\,d\phi' \end{aligned} \qquad (29)$$

Applying the same procedure, we obtain the apparent conductivity as

$$\begin{aligned} \sigma_a &= -\frac{V_R}{K} \\ &= \int_0^\infty d\rho' \int_{-\infty}^{\infty} dz'\sigma(\rho', z')g_P(\rho', z') \end{aligned} \qquad (30)$$

where

$$g_{\mathrm{P}} = \frac{2\pi L\rho'}{(\pi a)^3 N_{\mathrm{T}} I} A_{\phi\mathrm{R}} \int_0^{2\pi} \frac{\cos(\phi-\phi')}{\bar{r}_2}\, d\phi' \tag{31}$$

The function g_{P} is the exact definition of the geometrical factor. In comparison with Doll's geometrical factor, g_{P} depends not only on the tool configuration, but also on the formation conductivity, since the vector potential depends on the formation conductivity. The integral-form solution does not provide any computational advantage, since the differential equation for the vector potential $A_{\phi,\mathrm{R}}$ must still be solved. But it is now clear from Eq. (30) that the apparent conductivity is the result of a nonlinear convolution. Equation (30) also represents the starting point of inverse filtering techniques, which make use of both the R and X signals to reconstruct the formation conductivity.

Finding the vector potential $\boldsymbol{A}$ is still a challenge. Analytic solutions are available only for a few simple geometries. In most cases, we have to use numerical techniques such as the finite element method (FEM), finite difference method (FDM), numerical mode matching (NMM), or the volume integral equation method (VIEM). Interested readers may find Refs. 5 through 8 useful.

Previously, we mentioned that Doll's geometrical factor theory is only valid under some extreme conditions. In fact, it can be derived from the exact geometrical factor as a special case (4). In a homogeneous medium, the vector potential $A_{\phi,\mathrm{R}}$ can be calculated as

$$A_{\phi\mathrm{R}} \cong \frac{(\pi a^2)N_{\mathrm{T}} I}{4\pi} \frac{\rho'}{r_1^3} \Re e\{(1-ikr_1)e^{ikr_1}\} \tag{32}$$

The integration with respect to ϕ' in Eq. (31) can also be performed for $\bar{r}_2 \gg a$. The final result is

$$\sigma_a = \int_{-\infty}^{\infty}\int_0^{\infty} \sigma g_{\mathrm{D}}(\rho', z') \Re e\{(1-ikr_1)e^{ikr_1}\} d\rho'\, dz' \tag{33}$$

where

$$g_{\mathrm{D}}(\rho', z') = \frac{L}{2} \frac{\rho'^3}{r_1^3 r_2^3} \tag{34}$$

It is now clear that Doll's geometric factor and the exact geometric factor are the same when the medium is homogeneous and the wave number approaches zero.

So far we have discussed the basic theory of induction logging. We now use a simple example to show some practical concerns and briefly discuss the solutions. In Fig. 2, we show an apparent resistivity (the inverse of apparent conductivity) response of a commercial logging tool 6FF40 (trademark of the Schlumberger Company) in the Oklahoma benchmark. The black line is the formation resistivity, and the red line is the unprocessed data of 6FF40. We notice that the apparent resistivity data roughly indicate the variation of the true resistivity, but around 4850 ft the apparent resistivity R_{a} is much higher than the true resistivity R_{t}, which results from the "skin effect" (9). From 4927 to 4955 ft, R_{a} is substantially lower than R_{t}, which is caused by the so-called shoulder effect. The shoulder effect arises when two adjacent low-resistance layers generate strong signals, even though the tool is not in these two regions. Around 5000 ft, there are a number of thin layers, but the tool's response fails to indicate them. This failure results from the tool's limited resolution, which is represented in terms of the smallest thickness that can be identified by the tool.

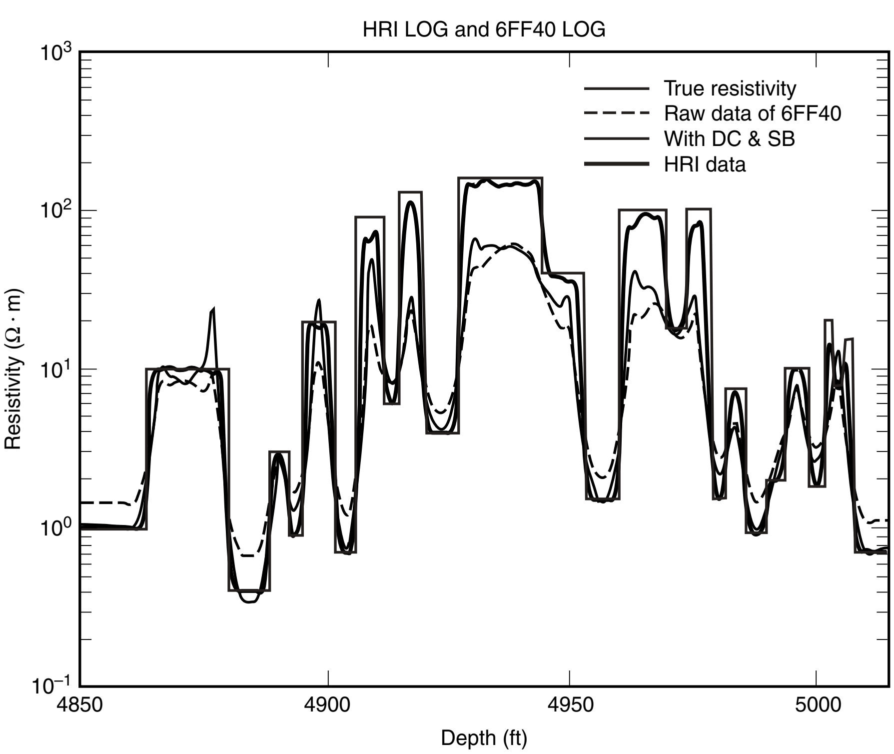

Figure 2. Apparent resistivity responses of a different tool in the Oklahoma benchmark. The improvement of resolution ability of the HR1 tool is significant.

The blue line is the processed 6FF40 data after skin effect boosting and a three-point deconvolution. Skin effect boosting is based on Eq. (19), which is solved iteratively for the true conductivity from the apparent conductivity. The three-point deconvolution is performed under the assumption that the convolution in Eq. (30) is almost linear (10). These two methods do improve the final results to some degree, but they also cause spurious artifacts observed near 4880 ft, since the two effects are considered separately. The green curve is the response of the HRI (high-resolution induction) tool (trademark of Halliburton) (11). A complex coil configuration is used to optimize the geometrical factor. After the raw data are obtained, a nonlinear deconvolution based on the X signal is performed. The improvement in the final results is significant.

Schlumberger Company recently released its AIT (array induction image tool), which uses eight induction-coil arrays operating at different frequencies (12). The deconvolutions are performed in both radial and vertical directions, and a quantitative two-dimensional image of formation resistivity is possible after a large number of measurements (13,14).

The aforementioned data processing techniques are based on the inverse deconvolution filter, which is computationally effective and easily run in real time on a logging truck computer. An alternative approach is to use inverse scattering theory, which is becoming increasingly practical and promising with the development of high-speed computers (8,15).

Besides the induction method, there are other methods, such as electrode methods and propagation methods. Induction methods are suitable for the fresh-water mud, oil-base mud, or air-filled boreholes, since the little or no conductivity in the borehole has a lesser effect on the measurement. If the mud is very conductive, it will generate a strong signal at the receiver and hence seriously degrade the tool's ability to make a deep reading. In such a case, electrode methods are preferable, since the conductive mud places the electrodes into better electrical contact with the formation. In the electrode methods, very low frequencies ($\ll$1000 Hz) are used and Laplace's equation is solved instead of the Helmholtz equation. The typical tools are DLL (dual laterolog) and SFL (spherical focusing log), both from Schlumberger. The dual laterolog is intended for both deep and shallow measurements, while the SFL is for shallow measurements (16–19).

In addition, there are many tools mounted on pads to perform shallow measurements on the borehole wall. These may be just button electrodes mounted on a metallic pad. Due to their small size, they have high resolution but a shallow depth of investigation. Their high resolution capability can be used to map out fine stratifications on the borehole wall. When four pads are equipped with these button electrodes, the resistivity logs they measure can be correlated to obtain the dip of a geological bed. An example of this is the SHDT (stratigraphic high-resolution dip meter tool), also from Schlumberger (20).

When an array of buttons are mounted on a pad, they can be used to generate a resistivity image of the borehole wall for formation evaluation, such as dips, cracks, and stratigraphy. Such a tool is called an FMS (formation microscanner) and is available from Schlumberger (21).

For oil-based mud the SHDT does not work well, and microinduction sensors have been mounted on a pad to dipping bed evaluation. Such a tool is known as the OBDT (oil-based mud dip meter tool) and is manufactured by Schlumberger (22,23).

Sometimes information is needed not only relating to the conductivity but also to the dielectric permittivity. In such cases, the EPT (electromagnetic wave propagation tool), from Schlumberger can be used. The working frequency of EPT can be as high as hundreds of megahertz to 1 GHz. At such high frequencies, the real part of ϵ' is dominant, as follows:

$$\epsilon' = \epsilon + i\frac{\sigma}{\omega} \tag{35}$$

EPT measurements provide information about dielectric permittivity and hence can better distinguish fresh water from oil. Water has a much higher dielectric constant ($80\epsilon_0$) compared to oil ($2\epsilon_0$). Phase delays at two receivers are used to infer the wave phase velocity and hence the permittivity. Interested readers can find materials on these methods in Refs. 24 and 25.

Other techniques in electrical well logging include the use of borehole radar. In such a case, a pulse is sent to a transmitting antenna in the borehole, and the pulse echo from the formation is measured at the receiver. Borehole radar finds application in salt domes where the electromagnetic loss is low. In addition, the nuclear magnetic resonance (NMR) technique can be used to detect the percentage of free water in a rock formation. The NMR signal in a rock formation is proportional to the spin echos from free protons that abound in free water. An example of such a tool is the PNMT (pulsed nuclear magnetic resonance tool), from Schlumberger (26).

GROUND PENETRATING RADAR

Another outgrowth of subsurface EM methods is ground penetrating radar (GPR). Because of its numerous advantages, GPR has been widely used in geological surveying, civil engineering, artificial target detection, and some other areas.

The GPR design is largely application oriented. Even though various systems have different applications and considerations, their advantages can be summarized as follows: (1) Because the frequency used in GPR is much higher than that used in the induction method, GPR has a higher resolution; (2) since the antennas do not need to touch the ground, rapid surveying can be achieved; (3) the data retrieved by some GPR systems can be interpreted in real time; and (4) GPR is potentially useful for organic contaminant detection and nondestructive detection (27–31).

On the other hand, GPR has some disadvantages, such as shallow investigation depth and site-specific applicability. The working frequency of GPR is much higher than that used in the induction method. At such high frequencies, the soil is usually very lossy. Even though there is always a tradeoff between the investigation depth and resolution, a typical depth is no more than 10 m and highly dependent on soil type and moisture content.

The working principle of GPR is illustrated in Fig. 3(a) (28). The transmitter T generates transient or continuous EM waves propagating in the underground. Whenever a change in the electrical properties of underground regions is encountered, the wave is reflected and refracted. The receiver R detects and records the reflected waves. From the recorded data, information pertaining to the depth, geometry, and material

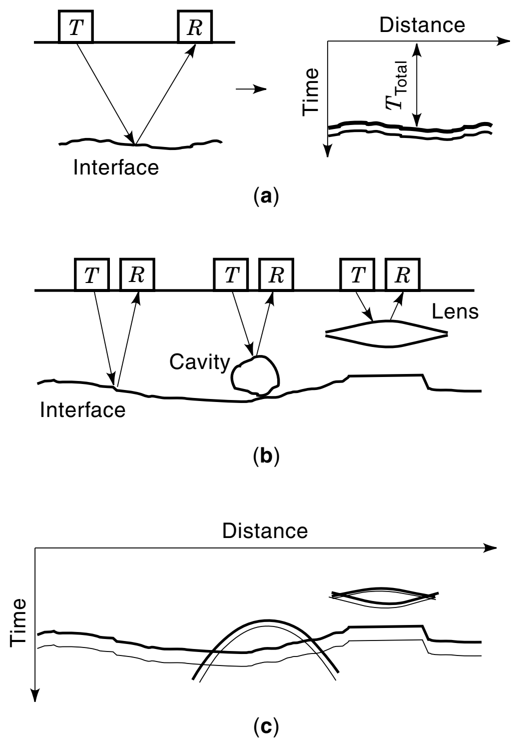

Figure 3. Working principle of the GPR. (Redrawn from Ref. 20.)

type can be obtained. As a simple example, we use Figs. 3(b) and 3(c) to illustrate how the data are recorded and interpreted. The underground contains one interface, one cavity, and one lens. At a single position, the receiver signals at different times are stacked along the time axis. After completing the measurement at one position, the procedure is iterated at all subsequent positions. The final results are presented in a two-dimensional map, which is called an echo sounder–type display. To locate objects or interfaces, we need to know the wave speed in the underground medium. The wave speed in a medium of relative dielectric permittivity ϵ_r is

$$C_s = \frac{C_0}{\sqrt{\epsilon_r}} \tag{36}$$

where $C_0 = 3 \times 10^8$ m/s. Usually, the transmitter and the receiver are close enough and thus the wave's path of propagation is considered to be vertical. The depth of the interface is approximated as

$$D = 0.5 \times (C_s \times T_{\text{total}}) \tag{37}$$

where T_{total} is the total wave propagation time.

A practical GPR system is much more complicated, and a block diagram of a typical baseband GPR system is shown in Fig. 4. Generally, a successful system design should meet the following requirements (27): (1) efficient coupling of the EM energy between antenna and ground; (2) adequate penetration with respect to the target depth; (3) sufficiently large return signal for detection; and (4) adequate bandwidth for the desired resolution and noise control.

The working frequency of typical GPR ranges from a few tens of megahertz to several gigahertz, depending on the application. The usual tradeoff holds: The wider the bandwidth, the higher the resolution but the shallower the penetration depth. A good choice is usually a tradeoff between resolution and depth. Soil properties are also critical in determining the penetration depth. It is observed experimentally that the attenuation of different soils can vary substantially. For example, dry desert and nonporous rocks have very low attenuation (about 1 dBm^{-1} at 1 GHz) while the attenuation of sea water can be as high as 300 dBm^{-1} at 1 GHz. Some typical

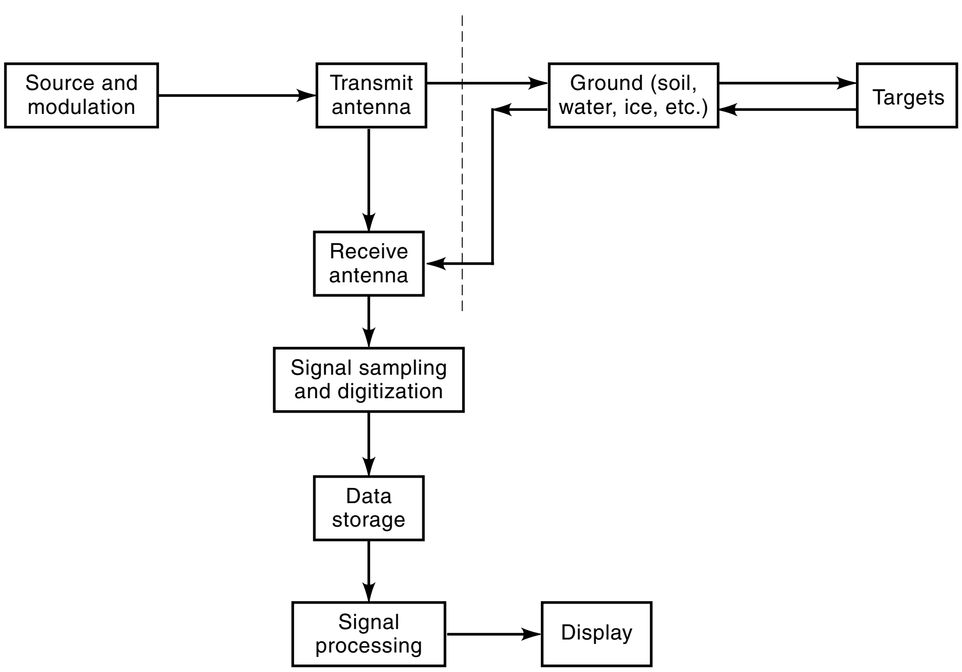

Figure 4. Block diagram showing operation of a typical baseband GPR system. (Redrawn from Ref. 19.)

applications and preferred operating frequencies are listed in Table 1 (27).

To meet the requirements of different applications, a variety of modulation schemes have been developed and can be classified in the following three categories: amplitude modulation (AM), frequency modulated continuous wave (FMCW), and continuous wave (CW). We will briefly discuss the advantages and limitations of each modulation scheme.

There are two types of AM transmission used in GPR. For investigation of low-conductivity medium, such as ice and fresh water, a pulse modulated carrier is preferred (32,33). The carrier frequency can be chosen as low as tens of megahertz. Since the reflectors are well spaced, a relatively narrow transmission bandwidth is needed. The receiver signal is demodulated to extract the pulse envelope. For shallow and high-resolution applications, such as the detection of buried artifacts, a baseband pulse is preferred to avoid the problems caused by high soil attenuation, since most of the energy is in the low-frequency band. A pulse train with a duration of 1 to 2 ns, a peak amplitude of about 100 V, and a repetition rate of 100 kHz is applied to the broadband antenna. The received signal is downconverted by sampling circuits before being displayed. There are three primary advantages of the AM scheme: (1) It provides a real-time display without the need for subsequent signal processing; (2) the measurement time is short; and (3) it is implemented with small equipment but without synthesized sources and hence is cost effective. But for the AM scheme, it is difficult to control the transmission spectrum, and the signal-to-noise ratio (SNR) is not as good as that of the FMCW method.

For the FMCW scheme, the frequency of the transmitted signal is continuously swept, and the receiver signal is mixed with a sample of transmitted signals. The Fourier transform of the received signal results in a time domain pulse that represents the receiver signal if a time domain pulse were transmitted. The frequency sweep must be linear in time to minimize signal degradation, and a stable output is required to facilitate signal processing. The major advantage of the FMCW scheme is easier control of the signal spectrum; the filter technique can be applied to obtain better SNR. A shortcoming of the FMCW system is the use of a synthesized frequency source, which means that the system is expensive and bulky. Additional data processing is also needed before the display (34,35).

Table 1. Desired Frequencies for Different Applications[a]

Material	Typical Desired Penetration Depth[b]	Approximate Maximum Frequency at Which Operation May Be Usefully Performed
Cold pure fresh-water ice	10 km	10 MHz
Temperate pure ice	1 km	2 MHz
Saline ice	10 m	50 MHz
Fresh water	100 m	100 MHz
Sand (desert)	5 m	1 GHz
Sandy soil	3 m	1 GHz
Loam soil	3 m	500 MHz
Clay (dry)	2 m	100 MHz
Salt (dry)	1 km	250 MHz
Coal	20 m	500 MHz
Rocks	20 m	50 MHz
Walls	0.3 m	10 GHz

[a] Redrawn from from Ref. 19.

[b] The figures used under this heading are the depths at which radar probing gives useful information, taking into account the attenuation normally encountered and the nature of the reflectors of interest.

A continuous wave scheme was used in the early development of GPR, but now it is mainly employed in synthetic aperture and subsurface holography techniques (36–38). In these techniques, measurements are performed at a single or a few well-spaced frequencies over an aperture at the ground surface. The wave front extrapolation technique is applied to reconstruct the underground region, with the resolution depending on the size of the aperture. Narrowband transmission is used and hence high-speed data capture is avoided. The difficulty of the CW scheme comes from the requirement for accurate scanning of the two-dimensional aperture. The operation frequencies should be carefully chosen to minimize resolution degradation (27).

Antennas play an important role in the system performance. An ideal antenna should introduce the least distortion on the signal spectrum or else one for which the modification can be easily compensated. Unlike the antennas used in the atmospheric radar, the antennas used in GPR should be considered as loaded. The radiation pattern of the GPR antenna can be quite different due to the strong interaction between the antenna and ground. Separate antennas for transmission and reception are commonly used, because it is difficult to make a switch that is fast enough to protect the receiver signal from the direct coupling signal. The direct breakthrough signals will seriously reduce the SNR and hence degrade the system performance. Moreover, in a separate-antenna system, the orientation of antennas can be carefully chosen to reduce further the cross-coupling level.

Except for the CW scheme, other modulation types require wideband transmission, which greatly restricts the choice of antenna. Four types of antennas, including element antennas, traveling wave antennas, frequency independent antennas, and aperture antennas, have been used in GPR designs. Element antennas, such as monopoles, cylindrical dipoles, and biconical dipoles, are easy to fabricate and hence widely used in GPR system. Orthogonal arrangement is usually chosen to maintain a low level of cross coupling. To overcome the limitation of narrow transmission bandwidth of thin dipole or monopole antennas, the distributed loading technique is used to expand the bandwidth at the expense of reduced efficiency (39–42).

Another commonly used antenna type is traveling wave antennas, such as long wire antennas, V-shaped antennas, and Rhombic antennas. The traveling wave antennas distinguish themselves from standing wave antennas in the sense that the current pattern is a traveling wave rather than a standing wave. Standing wave antennas, such as half-wave dipoles, are also referred to as resonant antennas and are narrowband, while traveling wave antennas are broadband. The disadvantage of traveling wave antennas is that half of the power is wasted at the matching resistor (43,44).

Frequency-independent antennas are often preferred in the impulse GPR system. It has been proved that if the antenna geometry is specified only by angles, its performance will be independent of frequency. In practice, we have to truncate the antenna due to its limited outer size and inner feeding region, which determine the lower bound and upper bound of the frequency, respectively. In general, this type of antenna will introduce nonlinear phase distortion, which results in an extended pulse response in the time domain (27,45). A phase correction procedure is needed if the antenna is used in a high-resolution GPR system.

A wire antenna is a one-dimensional antenna that has a small effective area and hence lower gain. For some GPR systems, higher gain or a more directive radiation pattern is sometimes required. Aperture antennas, such as horn antennas, are preferred because of their large effective area. A ridge design is used to improve the bandwidth and reduce the size. Ridged horns with gain better than 10 dBm over a range of 0.3 GHz to 2 GHz and VSWR lower than 1.5 over a range of 0.2 GHz to 1.8 GHz have been reported (46). Since many aperture antennas are fed via waveguides, the phase distortion associated with the different modulation schemes needs to be considered.

Generally, antennas used in GPR systems require broad bandwidth and linear phase in the operating frequency range. Since the antennas work in close proximity to the ground surface, the interaction between them must be taken into account.

Signal processing is one of the most important parts in the GPR system. Some modulation schemes directly give the time domain data while the signals of other schemes need to be demodulated before the information is available. Signal processing can be performed in the time domain, frequency domain, or space domain. A successful signal processing scheme usually consists of a combination of several kinds of processing techniques that are applied at different stages. Here, we outline some basic signal processing techniques involved in the GPR system.

The first commonly used method is noise reduction by time averaging. It is assumed that the noise is random, so that the noise can be reduced to $1/Nt$ by averaging N identical measurements spaced in time t. This technique only works for random noise but has no effects on the clutter.

Clutter reduction can be achieved by subtracting the mean. This technique is performed under the assumption that the statistics of the underground are independent of position. A number of measurements are performed at a set of locations over the same material type to obtain the mean, which can be considered as a measure of the system clutter.

The frequency filter technique is commonly used in the FMCW system. Signals that are not in the desired information bandwidth are rejected. Thus the SNR of FMCW scheme is usually higher than that of the AM scheme.

In some very lossy soils, the return signal is highly attenuated, which makes interpretation of the data difficult. If the material attenuation information is available, the results can be improved by exponentially weighting the time traces to counter the decrease in signal level due to the loss. In practice, this is done by using a specially designed amplifier. Caution is needed when using this method, since the noise can also increase in such a system (27).

MAGNETOTELLURIC METHODS

The basic idea of the magnetotelluric (MT) method is to use natural electromagnetic fields to investigate the electrical conductivity structure of the earth. This method was first proposed by Tikhonov in 1950 (47). In his paper, the author assumed that the earth's crust is a planar layer of finite conductivity lying upon an ideally conducting substrate, such that a simple relation between the horizontal components of the E and H fields at the surface can be found (48):

$$i\mu_0\omega H_x \cong E_y\gamma\cosh(\gamma l) \tag{38}$$

where

$$\gamma = (i\sigma\mu_0\omega)^{(1/2)} \tag{39}$$

The author used the data observed at Tucson (Arizona) and Zui (USSR) to compute the value of conductivity and thickness of the crust that best fit the first four harmonics. For Tucson, the conductivity and thickness were about 4.0×10^{-3} S/m and 1000 km, respectively. For Zui, the corresponding values are 3.0×10^{-1} S/m and 100 km.

The MT method distinguishes itself from other subsurface EM methods because very low frequency natural sources are used. The actual mechanisms of natural sources have been under discussion for a long time, but now it is well accepted that the sources of frequency above 1 Hz are thunderstorms while the sources below 1 Hz are due to the current system in the magnetosphere caused by solar activity. In comparison with other EM methods, the use of a natural source is a major advantage. The frequencies used range from 0.001 Hz to 10^4 Hz, and thus investigation depth can be achieved from 50 m to 100 m to several kilometers. Installation is much simpler and has less impact on the environment. The MT method has also proved very useful in some extreme areas where conventional seismic methods are expensive or ineffective. The main shortcomings of the MT method are limited resolution and difficulty in achieving a high SNR, especially in electrically noisy areas (49).

In MT measurements, the time-varying horizontal electrical and magnetic fields at the surface are recorded simultaneously. The data recorded in the time domain are first converted into frequency domain data by using a fast Fourier transform (FFT). An apparent conductivity is then defined as a function of frequency. To interpret the data, theoretical apparent conductivity curves are generated by the model studies. The model whose apparent conductivity curve best matches the measurement data is taken as an approximate model of the subsurface.

Since it is more convenient and meaningful to represent the apparent conductivity in terms of skin depth, we first introduce the concept of skin depth by studying a simple case. The model we use is shown in Fig. 5, which consists of a ho-

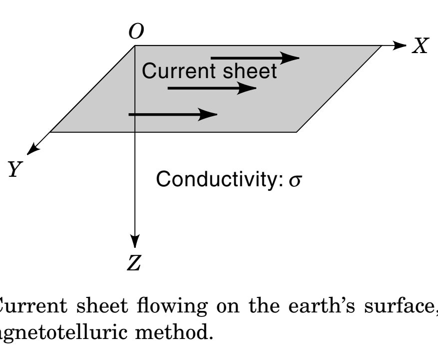

Figure 5. Current sheet flowing on the earth's surface, used to explain the magnetotelluric method.

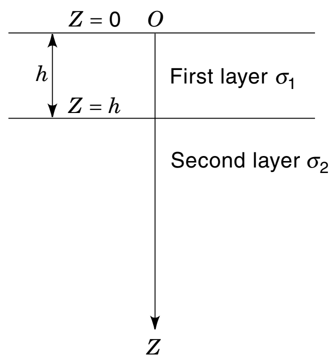

Figure 6. Two-layer model of the earth's crust, used to demonstrate the responses of the magnetotelluric method.

mogeneous medium with conductivity σ and a uniform current sheet flowing along the x direction in the xy plane. If the density of current at the ground ($z = 0$) is represented as (50)

$$I_x = \cos\omega t, I_y = I_z = 0 \tag{40}$$

then the current density at depth z is

$$I_x = e^{-z\sqrt{2\omega\mu\sigma}/2}\cos(\omega t - z\sqrt{2\omega\mu\sigma}), I_y = I_z = 0 \tag{41}$$

When z increases, we notice that the amplitude of the current decreases exponentially with respect to z; meanwhile the phase retardation progressively increases. To describe the amplitude attenuation, we introduce the skin depth p as (50)

$$p = \sqrt{\frac{2}{\omega\mu\sigma}} \tag{42}$$

where the current amplitude decreases to e^{-1} of the current at the surface. Since the unit in Eq. (42) is not convenient, some prospectors like to use the following formula:

$$p = \frac{1}{2\pi}\sqrt{10\rho T} \tag{43}$$

where T is the period in seconds, ρ is the resistivity in Ω/m, and the unit for p is km. The skin depth indicates the depth the wave can penetrate the ground. For example, if the resistivity of the underground is 10 S/m and the period of the wave is 3 s, the skin depth is 2.76 km. Subsurface methods seldom have such a great penetration depth.

The data interpretation of the MT method is based on the model studies. The earth is modeled as a two- or three-layer medium. For a two-layer model as shown in Fig. 6, the general expression for the field can be written as (50)
$0 \le z \le h$:

$$E_z = Ae^{a\sqrt{\sigma_1}z} + be^{-a\sqrt{\sigma_1}z} \tag{44a}$$

$$H_y = e^{i\pi/4}\sqrt{2\sigma_1 T}\,[-Ae^{a\sqrt{\sigma_1}z} + Be^{-a\sqrt{\sigma_1}z}] \tag{44b}$$

$h \le z \le \infty$:

$$E_x = e^{-a\sqrt{\sigma_2}z} \tag{45a}$$

$$H_x = e^{i\pi/4}\sqrt{2\sigma_2 T}e^{-a\sqrt{\sigma}z} \tag{45b}$$

where h is the thickness of upper layer, and σ_1, σ_2 are the conductivities of the upper and lower layers, respectively. Matching the boundary conditions at $z = h$, we have

$$A = \frac{\sqrt{\sigma_1} - \sqrt{\sigma_2}}{2\sqrt{\sigma_1}}\, e^{-ah(\sqrt{\sigma_1}+\sqrt{\sigma_2})} \tag{46}$$

$$B = \frac{\sqrt{\sigma_1} + \sqrt{\sigma_2}}{2\sqrt{\sigma_1}}\, e^{ah(\sqrt{\sigma_1}-\sqrt{\sigma_2})} \tag{47}$$

Since we are interested in the ratio between the E and H field on the surface, Eq. (44) can be rewritten for $z = 0$ as

$$\frac{E_x}{H_y} = \frac{1}{\sqrt{2\sigma_1 T}}\frac{M}{N}\, e^{-i(\pi/4+\phi+\psi)} \tag{48}$$

where M, N, ϕ, and ψ satisfy the following equations:

$$M\cos\phi = \left(\frac{1}{p_1}\cosh\frac{h}{p_1} + \frac{1}{p_2}\sinh\frac{h}{p_1}\right)\cos\frac{h}{p_1} \tag{49a}$$

$$M\sin\phi = \left(\frac{1}{p_1}\sinh\frac{h}{p_1} + \frac{1}{p_2}\cosh\frac{h}{p_1}\right)\sin\frac{h}{p_1} \tag{49b}$$

$$N\cos\psi = \left(\frac{1}{p_1}\sinh\frac{h}{p_1} + \frac{1}{p_2}\cosh\frac{h}{p_1}\right)\cos\frac{h}{p_1} \tag{49c}$$

$$N\sin\psi = \left(\frac{1}{p_1}\cosh\frac{h}{p_1} + \frac{1}{p_2}\sinh\frac{h}{p_1}\right)\sin\frac{h}{p_1} \tag{49d}$$

where p_1, p_2 are the skin depths of upper and lower layers, respectively.

For a multilayer medium, after applying the same procedure, we can obtain exactly the same relation between E_x and H_y as shown in Eq. (48) except that the expressions for M, N, ϕ, and ψ are much more complicated. Because of this similarity, we have

$$\left|\frac{E_x}{H_y}\right| = \frac{1}{\sqrt{2\sigma_a T}} = \frac{M}{N}\frac{1}{\sqrt{2\sigma_1 T}} \tag{50}$$

where σ_a is defined as the apparent conductivity. If the medium is homogeneous, the apparent conductivity is equal to the true conductivity. In a multilayer medium the apparent conductivity is an average effect of all layers.

To obtain a better understanding of the preceding formulas, we first study two two-layer models and their corresponding apparent conductivity curves, as shown in Fig. 7 (51). At

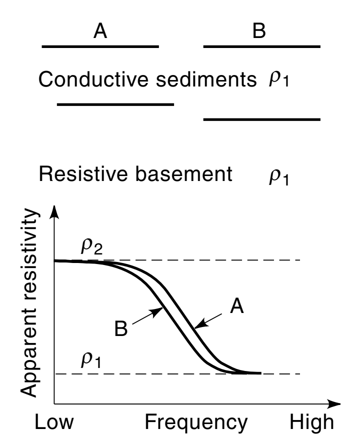

Figure 7. Diagrammatic two-layer apparent resistivity curves for the models shown. (Redrawn from Ref. 43.)

very low frequencies, the wave can easily penetrate the upper layer, and thus its conductivity has little effect on the apparent conductivity. Consequently, the apparent resistivity approaches the true resistivity of lower layer. As the frequency increases, less energy can penetrate the upper layer due to the skin effect, and thus the effect from the upper layer is dominant. As a result, the apparent resistivity is asymptotic to ρ_1. Comparing the two curves, we note that both of them change smoothly, and for the same frequency, case A has lower apparent resistivity than case B, since the conductive sediments of case B are thicker.

Our next example is a three-layer model as shown in Fig. 8 (51). The center layer is more conductive than the two adjacent ones. As expected, the curve approaches ρ_1 and ρ_2 at each end. The existence of the center conductive bed is obvious from the curve, but the apparent resistivity never reaches the true resistivity of center layer, since its effect is averaged by the effects from the other two layers.

So far we have only discussed the horizontally layered medium, which is a one-dimensional model. In practice, two-dimensional or even three-dimensional structures are often encountered. In a 2-D case, the conductivity changes not only along the z direction but also along one of the horizontal directions. The other horizontal direction is called the "strike" direction. If the strike direction is not in the x or y direction, we obtain a general relation between the horizontal field components as (51)

$$E_x = Z_{xx}H_x + Z_{xy}H_y \tag{51a}$$

$$E_y = Z_{yx}H_x + Z_{yy}H_y \tag{51b}$$

Since E_x, E_y, H_x, and H_y are generally out of phase, $Z_{i,j}$ are complex numbers. It can also be shown that $Z_{i,j}$ have the following properties:

$$Z_{xx} + Z_{yy} = 0 \tag{52}$$

$$Z_{xy} - Z_{yx} = \text{constant} \tag{53}$$

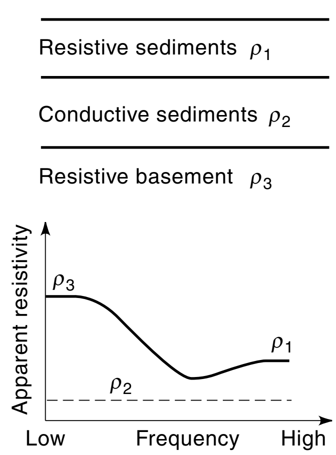

Figure 8. Diagrammatic three-layer apparent resistivity curve for the model shown. (Redrawn from Ref. 43.)

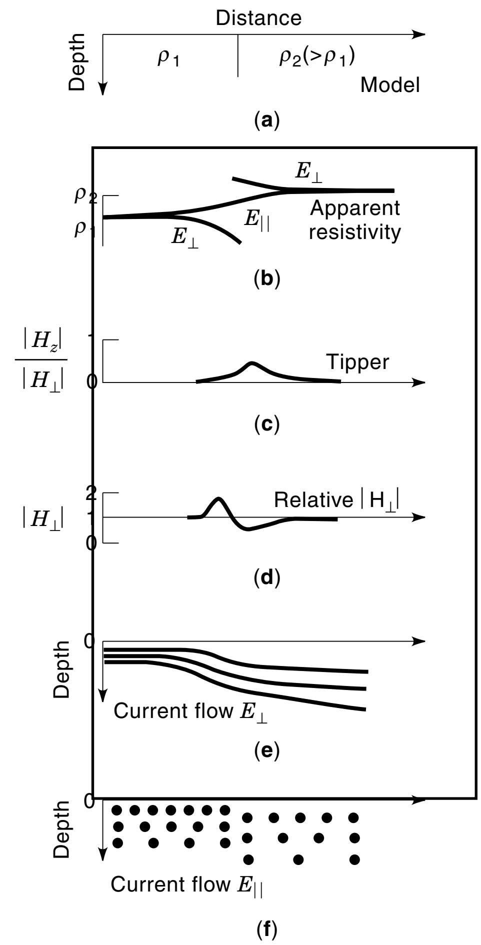

Figure 9. Diagrammatic response curves for a simple vertical contact at frequency f. (Redrawn from Ref. 43.)

A simple vertical layer model and its corresponding curves are shown in Fig. 9 (51). In Fig. 9(b), the apparent resistivity with respect to $E_\|$ changes slowly from $\rho 1$ to $\rho 2$ due to the continuity of $H_\perp$ and $E_\|$ across the interface. On the other hand, the apparent resistivity corresponding to $E_\perp$ has an abrupt change across the contact, since the $E_\perp$ is discontinuous at the interface. The relative amplitude of $H_\perp$ varies significantly around the interface and approaches a constant at a large distance, as shown in Fig. 9(d). This is caused by the change in current density near the interface, as shown in Fig. 9(f). We also observe that H_z appears near the interface, as shown in Fig. 9(c). The reason is that the partial derivative of $E_\|$ with respect to $\perp$ direction is nonzero.

We have discussed the responses in some idealized models. For more complicated cases, their response curves can be obtained by forward modeling. Since the measurement data are in the time domain, we need to convert them into the frequency domain data by using a Fourier transform. In practice, five components are measured. There are four unknowns in Eqs. (51a) and (51b), but only two equations. This difficulty can be overcome by making use of the fact that $Z_{i,j}$ changes very slowly with frequency. In fact, $Z_{i,j}$ is computed as an average over a frequency band that contains several frequency sample points. A commonly used method is given in Ref. 52, according to which Eq. (51a) is rewritten as

$$\langle E_x A^* \rangle = Z_{xx} \langle H_x A^* \rangle + Z_{xy} \langle H_y A^* \rangle \tag{54}$$

and

$$\langle E_x B^* \rangle = Z_{xx} \langle H_x B^* \rangle + Z_{xy} \langle H_y B^* \rangle \tag{55}$$

where A^* and B^* are the complex conjugates of any two of the horizontal field components. The cross powers are defined as

$$\langle AB^* \rangle (\omega_1) = \frac{1}{\Delta\omega} \int_{\omega_1 - (\Delta\omega/2)}^{\omega_1 + (\Delta\omega/2)} AB^* \, d\omega \tag{56}$$

There are six possible combinations, and the pair (H_x, H_y) is preferred in most cases due to its greater degree of independence. Solving Eqs. (54) and (55), we have

$$Z_{xx} = \frac{\langle E_x A^* \rangle \langle H_y B^* \rangle - \langle E_x B^* \rangle \langle H_y A^* \rangle}{\langle H_x A^* \rangle \langle H_y B^* \rangle - \langle H_x B^* \rangle \langle H_y A^* \rangle} \tag{57a}$$

and

$$Z_{xy} = \frac{\langle E_x A^* \rangle \langle H_x B^* \rangle - \langle E_x B^* \rangle \langle H_X A^* \rangle}{\langle H_y A^* \rangle \langle H_x B^* \rangle - \langle H_y B^* \rangle \langle H_x A^* \rangle} \tag{57b}$$

Applying the same procedure to Eq. (51b), we have

$$Z_{yx} = \frac{\langle E_y A^* \rangle \langle H_y B^* \rangle - \langle E_y B^* \rangle \langle H_y A^* \rangle}{\langle H_x A^* \rangle \langle H_y B^* \rangle - \langle H_x B^* \rangle \langle H_y A^* \rangle} \tag{57c}$$

and

$$Z_{yy} = \frac{\langle E_y A^* \rangle \langle H_x B^* \rangle - \langle E_y B^* \rangle \langle H_x A^* \rangle}{\langle H_y A^* \rangle \langle H_x B^* \rangle - \langle H_y B^* \rangle \langle H_x A^* \rangle} \tag{57d}$$

After obtaining $Z_{i,j}$, they can be substituted into Eqs. (51a) and (51b) to solve for the other pair (E_x, E_y), which is then used to check the measurement data. The difference is due either to noise or to measurement error. This procedure is usually used to verify the quality of the measured data.

AIRBORNE ELECTROMAGNETIC METHODS

Airborne EM methods (AEM) are widely used in geological surveys and prospecting for conductive ore bodies. These methods are suitable for large area surveys because of their speed and cost effectiveness. They are also preferred in some areas where access is difficult, such as swamps or ice-covered areas. In contrast to ground EM methods, airborne EM methods are usually used to outline large-scale structures while ground EM methods are preferred for more detailed investigations (53).

The difference between airborne and ground EM systems results from the technical limitations inherent in the use of aircraft. The limited separation between transmitter and receiver determines the shallow investigation depth, usually from 25 m to 75 m. Even though greater penetration depth can be achieved by placing the transmitter and receiver on different aircraft, the disadvantages are obvious.

The transmitters and receivers are usually 200 ft to 500 ft above the surface. Consequently, the amplitude ratio of the primary field to the secondary field becomes very small and thus the resolution of airborne EM methods is not very high. The operating frequency is usually chosen from 300 Hz to 4000 Hz. The lower limit is set by the transmission effectiveness, and the upper limit is set by the skin depth.

Based on different design principles and application requirements, many systems have been built and operated all over the world since 1940s. Despite the tremendous diversity, most airborne EM systems can be classified in one of the following categories according to the quantities measured: phase component measuring systems, quadrature systems, rotating field systems, and transient response systems (54).

For a phase component measuring system, the in-phase and quadrature components are measured at a single frequency and recorded as parts per million (ppm) of the primary field. In the system design, vertical loop arrangements are preferred, since they are more sensitive to the steeply dipping conductor and less sensitive to the horizontally layered conductor (55). Accurate maintenance of transmitter-receiver separation is essential and can be achieved by fixing the transmitter and receiver at the two wing tips. Once this requirement is satisfied, a sensitivity of a few ppm can be achieved (54). A diagram of the phase component measuring system is shown in Fig. 10 (55). A balancing network associated with the reference loop is used to buck the primary field at the receiver. The receiver signal is then fed to two phase-sensitive demodulators to obtain the in-phase and quadrature components. Low-pass filters are used to reject very-high-frequency signals that do not originate from the earth. The data are interpreted by matching the curves obtained from the modeling. Some response curves of typical structures are given in Ref. 56.

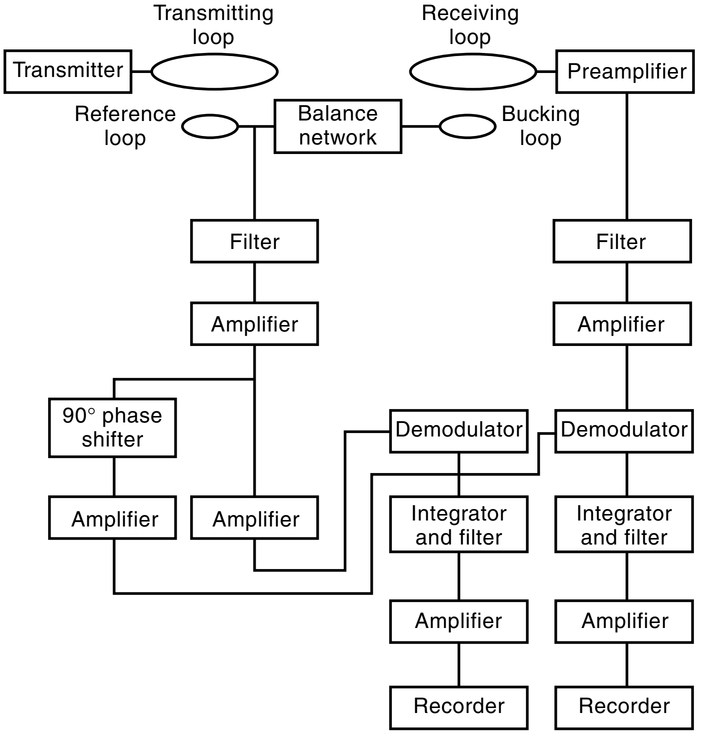

Figure 10. Block diagram showing operation of a typical phase component measuring system. (Redrawn from Ref. 43.)

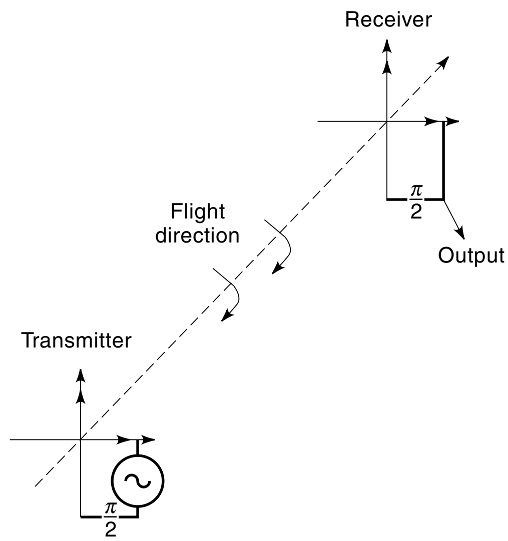

Figure 11. Working principle of the rotary field AEM system. (Redrawn from Ref. 50.)

The quadrature system employs a horizontal coil placed on the airplane as a transmitter and a vertical coil towed behind the plane as a receiver. The vertical coil is referred to as a "towed bird." Since only the quadrature component is measured, the separation distance is less critical. To reduce the noise further, an auxiliary horizontal coil, powered with a current 90 degrees out of phase with respect to the main transmitter current, is used to cancel the secondary field caused by the metal body of the aircraft. Since the response at a single frequency may have two interpretations, two frequencies are used to eliminate the ambiguity. The lower frequency is about 400 Hz and the higher one is chosen from 2000 Hz to 2500 Hz. The system responses in different environments can be obtain by model studies. Reference 57 gives a number of curves for thin sheets and shows the effects of variation in depth, dipping angle, and conductivity.

In an airborne system, it is hard to control the relative rotation of receiver and transmitter. The rotating field method is introduced to overcome this difficulty. Two transmitter coils are placed perpendicular to each other on the plane, and a similar arrangement is used for the receiver. The two transmitters are powered with current of the same frequency shifted 90 degrees out of phase, so that the resultant field rotates about the axis, as shown in Fig. 11 (58). The two receiver signals are phase shifted by 90 degrees with respect to each other, and then the in-phase and quadrature differences at the two receivers are amplified and recorded by two different channels. Over a barren area, the outputs are set to zero. When the system is within a conducting zone, anomalies in the conductivity are indicated by nonzero outputs in both the in-phase and quadrature channels. The noise introduced by the fluctuation of orientation can be reduced by this scheme, but it is relatively expensive and the data interpretation is complicated by the complex coil system (58).

The fundamental problem of airborne EM systems is the difficulty in detecting the relatively small secondary field in the presence of a strong primary field. This difficulty can be alleviated by using the transient field method. A well-known system based on the transient field method is INPUT (INduced PUlsed Transient) (59), which was designed by Barringer during the 1950s. In the INPUT system, a large horizontal transmitting coil is placed on the aircraft and a vertical receiving coil is towed in the bird with the axis aligned with the flight direction.

The working principle of INPUT is shown in Fig. 12 (60). A half sine wave with a duration of about 1.5 ms and quiet period of about 2.0 ms is generated as the primary field, as shown in Fig. 12(a). If there are no conducting zones, the current in the receiver is induced only by the primary field, as shown in Fig. 12(b). In the presence of conductive anomalies, the primary field will induce an eddy current. After the primary field is cut off, the eddy current decays exponentially. The duration of the eddy current is proportional to the conductivity anomalies, as shown in Fig. 12(c). The higher the conductivity, the longer the duration time. The decay curve in the quiet period is sampled successively in time by six channels and then displayed on a strip, as shown in Fig. 13. As we can see, the distortion caused by a good conductor ap-

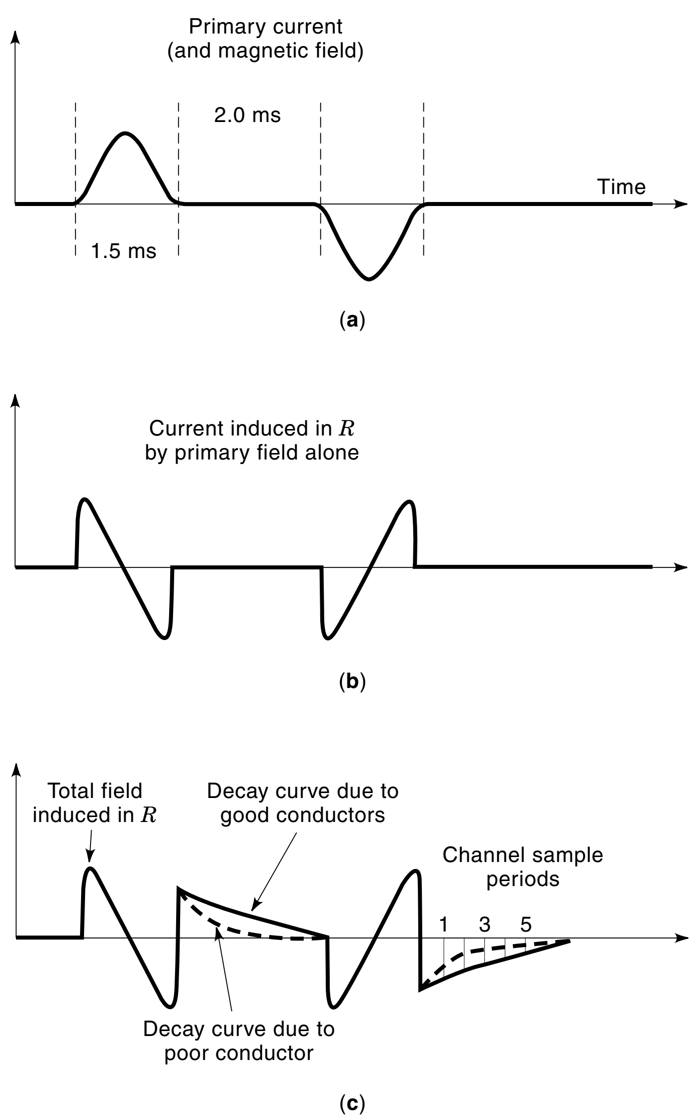

Figure 12. Working principle of the INPUT system. (Redrawn from Ref. 52.)

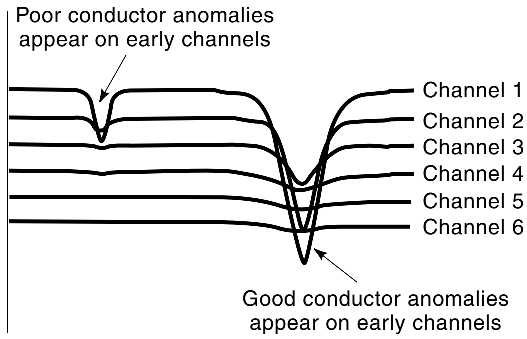

Figure 13. Responses of different anomalies appearing on different channels. (Redrawn from Ref. 52.)

pears in all the channels, while the distortion corresponding to a poor conductor only registers on the early channels.

Since the secondary field can be measured more accurately in the absence of the primary field, transient systems provide greater investigation depths, which may reach 100 m under favorable conditions. In addition, they can also provide a direct indication of the type of conductor encountered (58).

On the other hand, this system design gives rise to other problems inherent in the transient method. Since the eddy current in the quiet period becomes very small, a more intense source has to be used in order to obtain the same signal level as that in continuous wave method. The circuitry for the transient system is much more complicated, and it is more difficult to reject the noise due to the wideband property of the transient signal.

BIBLIOGRAPHY

1. C. M. Swift, Jr., Fundamentals of the electromagnetic method, in M. N. Nabighian (ed.), *Electromagnetic Methods in Applied Geophysics: Theory,* Tulsa, OK: Society of Exploration Geophysicists, 1988.
2. H. G. Doll, Introduction to induction logging and application to logging of wells drilled with oil based mud, *J. Petroleum Tech.,* **1**: 148–162, 1949.
3. J. H. Moran and K. S. Kunz, Basic theory of induction logging and application to study of two-coil sondes, *Geophysics.,* **27** (6): 829–858, 1962.
4. S. J. Thandani and H. E. Hall, Propagated geometric factors in induction logging, *Trans. SPWLA,* **2**: paper WW, 1981.
5. B. Anderson, Induction sonde response in stratified medium, *The Log Analyst,* **XXIV** (1): 25–31.
6. W. C. Chew, Response of a current loop antenna in an invaded borehole, *Geophysics,* **49**: 81–91, 1984.
7. J. R. Lovell, *Finite Element Method in Resistivity Logging,* Ridgefield, CT: Schlumberger Technology Corporation, 1993.
8. W. C. Chew and Q. H. Liu, Inversion of induction tool measurements using the distorted Born iterative method and CG-FFHT, *IEEE Trans. Geosci. Remote Sens.,* **32** (4): 878–884, 1994.
9. S. Gianzero and B. Anderson, A new look at skin effect, *The Log Analyst,* **23** (1): 20–34, 1982.
10. L. C. Shen, Effects of skin-effect correction and three-point deconvolution on induction logs, *The Log Analyst,* July–August issue, pp. 217, 1989.
11. R. Strickland et al., New developments in the high resolution induction log, *Trans. SPWLA,* **2**: paper ZZ, 1991.
12. T. D. Barber and R. A. Rosthal, Using a multiarray induction tool to achieve high resolution logs with minimum environmental effects, *Trans. SPE,* paper SPE 22725, 1991.
13. G. P. Grove and G. N. Minerbo, An adaptive borehole correction scheme for array induction tools, presented at the *32nd Ann. SPWLA Symposium,* Midland, TX, 1991.
14. Schlumberger Educational Services, *AIT Array Induction Image Tool,* 1992.
15. R. Freedman and G. N. Minerbo, Maximum entropy inversion of induction log data, *Trans. SPE,* **5**: 381–394, paper SPE 19608, 1989.
16. S. J. Grimaldi, P. Poupon, and P. Souhaite, The daul laterolog-R_{xo} tool, *Trans. SPE,* **2**: 1–12, paper SPE 4018, 1972.
17. R. Chemali et al., The sholder bed effect on the daul laterolog and its variation with the resistivity of the borehole fluid, *Trans. SPWLA,* paper UU, 1983.
18. Q. Liu, B. Anderson, and W. C. Chew, Modeling low frequency electrode-type resistivity tools in invaded thin beds, *IEEE Trans. Geosci. Remote Sens.,* **32** (3): 494–498, 1994.
19. B. Anderson and W. C. Chew, SFL interpretation using high speed synthetic computer generated logs, *Trans. SPWLA,* paper K, 1985.
20. Y. Chauvel, D. A. Seeburger, and C. O. Alfonso, Application of the SHDT stratigraphic high resolution dipmeter to the study of depositional environments, *Trans. SPWLA,* paper G, 1984.
21. A. R. Badr and M. R. Ayoub, Study of a complex carbonate reservoir using the Formation MicroScanner (FMS) tool, *Proc 6th Middleeast Oil Show,* Bahrain, March, 1989, pp. 507–516.
22. R. L. Kleinberg et al., Microinduction sensor for the oil-based mud dipmeter, *SPE Formation Evaluation,* vol. 3, pp. 733–742, December 1988.
23. W. C. Chew and R. L. Kleinberg, Theory of microinduction measurements, *IEEE Trans. Geosci. Remote Sens.,* **26**: 707–719, 1988.
24. W. C. Chew and S. Gianzero, Theoretical investigation of the electromagnetic wave propagation tool, *IEEE Trans. Geosci. Remote Sens.,* **GE-19**: 1–7, 1981.
25. W. C. Chew et al., An effective solution for the response of electrical welllogging tool in a complex environment, *IEEE Trans. Geosci. Remote Sens.,* **29**: 303–313, 1991.
26. D. D. Griffin, R. L. Kleinberg, and M. Fukuhara, Low-frequency NMR spectrometer measurement, *Science & Technology,* **4**: 968–975, 1993.
27. D. J. Daniels, D. J. Gunton, and H. F. Scott, Introduction to subsurface radar, *IEEE Proc.,* **135**: 278–320, 1988.
28. D. K. Butler, Elementary GPR overview, *Proc. Government Users Workshop on Ground Penetrating Radar Application and Equipment,* pp. 25–30, 1992.
29. W. H. Weedon and W. C. Chew, Broadband microwave inverse scattering for nondestructive evaluation, *Proc. Twentieth Annu. Review Progress Quantitative Nondestructive Evaluation,* Drunswick, ME, 1993.
30. F. C. Chen and W. C. Chew, Time-domain ultra-wideband microwave imaging radar system, *Proc. IEEE Instrum. Meas. Technol. Conf.,* St. Paul, MN, pp. 648–650, 1998.
31. F. C. Chen and W. C. Chew, Development and testing of the time-domain microwave nondestructive evaluation system, *Review of Progress in Quantitative Evaluation,* vol. 17, New York: Plenum, 1998, pp. 713–718.
32. M. Walford, Exploration of temperate glaciers, *Phys. Bull.,* **36**: 108–109, 1985.
33. D. K. Hall, A review of the utility of remote sensing in Alaskan permafrost studies, *IEEE Trans. Geosci. Remote Sens.,* **GE-20**: 390–394, 1982.

34. A. Z. Botros et al., Microwave detection of hidden objects in walls, *Electron. Lett.,* **20**: 379–380, 1984.
35. P. Dennis and S. E. Gibbs, Solid-state linear FM/CW radar systems—their promise and their problems, *Proc. IEEE MTT Symp.,* 1974, pp. 340–342.
36. A. P. Anderson and P. J. Richards, Microwave imaging of subsurface cylindrical scatters from cross-polar backscatter, *Electron. Lett.,* **13**: 617–619, 1977.
37. K. Lizuka et al., Hologram matrix radar, *Proc. IEEE,* **64**: 1493–1504, 1976.
38. N. Osumi and K. Ueno, Microwave holographic imaging method with improved resolution, *IEEE Trans. Antennas Propag.,* **AP-32**: 1018–1026, 1984.
39. M. C. Bailey, Broad-band half-wave dipole, *IEEE Trans. Antennas Propag.,* **AP-32**: 410–412, 1984.
40. R. P. King, Antennas in material media near boundaries with application to communication and geophysical exploration, *IEEE Trans. Antennas Propag.,* **AP-34**: 483–496, 1986.
41. M. Kanda, A relatively short cylindrical broadband antenna with tapered resistive loading for picosecond pulse measurements, *IEEE Trans. Antennas Propag.,* **AP-26**: 439–447, 1978.
42. C. A. Balanis, *Antenna Theory,* chapter 9, New York: Wiley, 1997.
43. P. Degauque and J. P. Thery, Electromagnetic subsurface radar using the transient radiated by a wire antenna, *IEEE Trans. Geosci. Remote Sens.,* **GE-24**: 805–812, 1986.
44. C. A. Balanis, *Antenna Theory,* chapter 10, New York: Wiley, 1997.
45. C. A. Balanis, *Antenna Theory,* chapter 11, New York: Wiley, 1997.
46. J. L. Kerr, Short axial length broadband horns, *IEEE Trans. Antennas Propag.,* **AP-21**: 710–714, 1973.
47. A. N. Tikhonov, Determination of the electrical characteristics of the deep strate of the earth's crust, *Proc. Acad. Sci.,* USSR, **83** (2): 295–297, 1950.
48. J. R. Wait, Theory of magneto-telluric field, *J. Res. Natl. Bur. Stand.-D,* Radio Propagation, **66D**: 509–541, 1962.
49. K. Vozoff, The magnetotelluric method, in M. N. Nabighian (ed.), *Electromagnetic Methods in Applied Geophysics: Application,* Tulsa, OK: Society of Exploration Geophysicists, 1988.
50. L. Cagniard, Basic theory of the magneto-telluric method of geophysical prospecting, *Geophysics.,* **18**: 605–635, 1952.
51. K. Vozoff, The magnetotelluric method in the exploration of sedimentary basins, *Geophysics.,* **37**: 98–141, 1972.
52. T. Madden and P. Nelson, A defense of Cagniard's magnetotelluric method, *Geophysics Reprinted Series No. 5: Magnetotelluric Methods,* Tulsa, OK: Society of Exploration Geophysicists, 1985, pp. 89–102.
53. G. J. Palacky and G. F. West, Airborne electromagnetic methods, in M. N. Nabighian (ed.), *Electromagnetic Methods in Applied Geophysics: Theory,* Tulsa, OK: Society of Exploration Geophysicists, 1988.
54. J. C. Gerkens, *Foundation of Exploration Geophysics,* New York: Elsevier, 1989.
55. G. V. Keller and F. Frischknecht, *Electrical Methods in Geophysical Prospecting,* New York: Pergamon, 1966.
56. D. Boyd and B. C. Roberts, Model experiments and survey results from a wing tip-mounted electromagnetic prospecting system, *Geophys. Pro.,* **9**: 411–420, 1961.
57. N. R. Patterson, Experimental and field data for the dual frequency phase-shift method of airborne electromagnetic prospecting, *Geophysics,* **26**: 601–617, 1961.
58. P. Kearey and M. Brooks, *An Introduction to Geophysical Exploration,* Boston, MA: Blackwell Scientific, 1984.
59. A. R. Barringer, The INPUT electrical pulse prospecting system, *Min. Cong. J.,* **48**: 49–52, 1962.
60. A. E. Beck, *Physical Principles of Exploration Methods,* New York: Macmillan, 1981.

S. Y. Chen
W. C. Chew
University of Illinois at Urbana-Champaign